iScience

CellPress
OPEN ACCESS

Article

RAD21 deficiency drives corneal to scleral differentiation fate switching via upregulating WNT9B

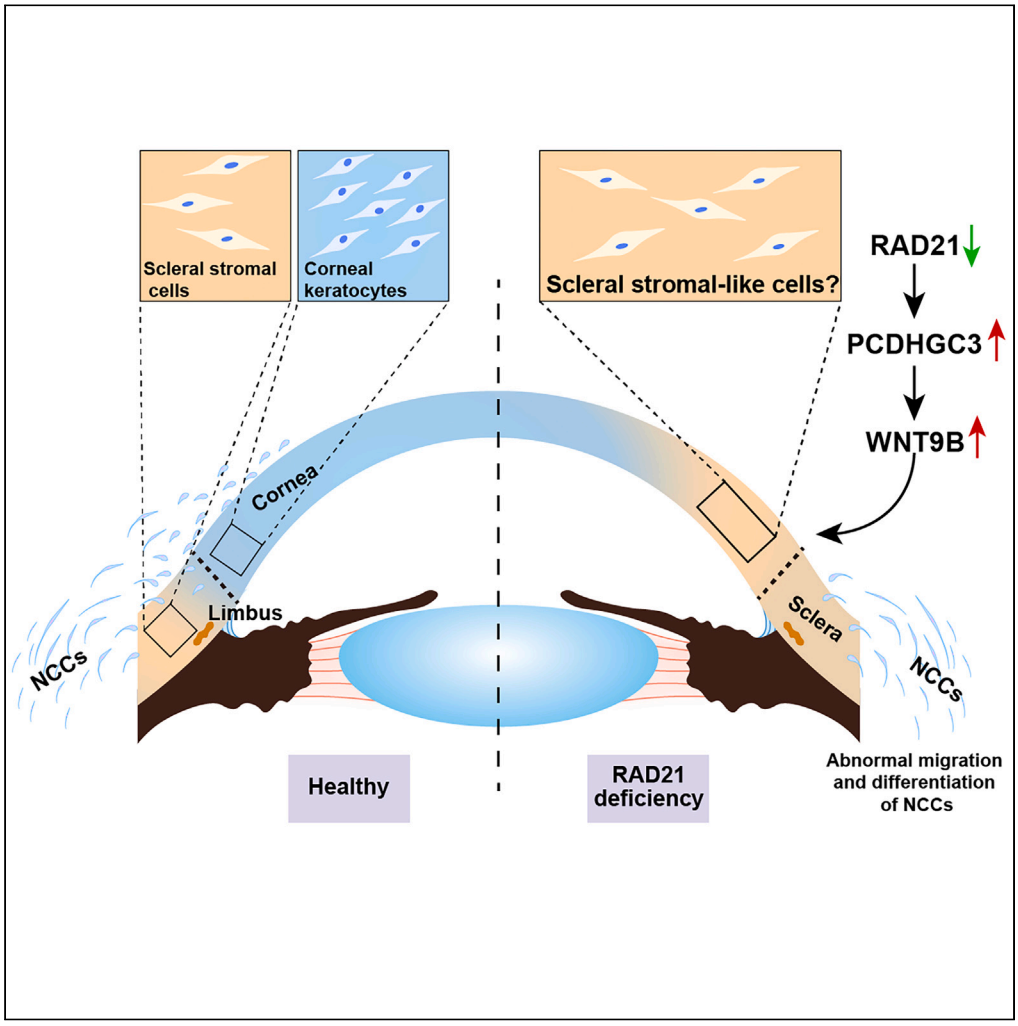

Hongyan Liu, Benxiang Qi, Guanghui Liu, ..., Wai Kit Chu, Qingjun Zhou, Bi Ning Zhang

zbnxtt@gmail.com

Highlights

Established a stable differentiation protocol from hESCs to corneal keratocytes

RAD21 deficiency affected the proliferation and migration ability of NCCs

Increased scleral markers after RAD21 knockdown during NCC differentiation to cornea

WNT9B is a crucial mediator during ocular NCC differentiation

Liu et al., iScience 27, 109875
June 21, 2024
https://doi.org/10.1016/j.isci.2024.109875

iScience

CellPress
OPEN ACCESS

Article

RAD21 deficiency drives corneal to scleral differentiation fate switching via upregulating WNT9B

Hongyan Liu,[1,2,3] Benxiang Qi,[2,3,4] Guanghui Liu,[5] Haoyun Duan,[2,3,4] Zongyi Li,[2,3,4] Zhaoying Shi,[5] Yonglong Chen,[5] Wai Kit Chu,[6] Qingjun Zhou,[2,3,4] and Bi Ning Zhang[2,3,4,7,*]

SUMMARY

The cornea and sclera are distinct adjacent tissues, yet their stromal cells originate from common neural crest cells (NCCs). Sclerocornea is a disease characterized by an indistinguishable boundary between the cornea and sclera. Previously, we identified a *RAD21* mutation in a sclerocornea pedigree. Here, we investigated the impacts of *RAD21* on NCC activities during eye development. *RAD21* deficiency caused upregulation of *PCDHGC3*. Both *RAD21* knockdown and *PCDHGC3* upregulation disrupted the migration of NCCs. Transcriptome analysis indicated that *WNT9B* had 190.9-fold higher expression in scleral stroma than in corneal stroma. *WNT9B* was also significantly upregulated by both *RAD21* knockdown and *PCDHGC3* overexpression, and knock down of *WNT9B* rescued the differentiation and migration of NCCs with *RAD21* deficiency. Consistently, overexpressing *wnt9b* in *Xenopus tropicalis* led to ocular developmental abnormalities. In summary, WNT9B is a determinant factor during NCC differentiation into corneal keratocytes or scleral stromal cells and is affected by RAD21 expression.

INTRODUCTION

Organ development and formation depend on dynamic adjustments in gene expression profiles to differentiate into specific cell lineages.[1–3] These processes intricately link to the three-dimensional (3D) chromatin structure,[4] with cohesin playing a pivotal role in facilitating the formation of chromatin loops and regulating the activity of core pluripotency genes.[5–7] Loss of cohesin complex subunits Rad21 and Nipped-B triggers the premature differentiation of intestinal stem cells to enterocytes in *Drosophila*.[8] The 3D genome undergoes dynamic alterations during development, facilitated by chromatin-organized topologically associated domains (TADs).[9,10] Cohesin and CCCTC-binding factor (CTCF) jointly contribute to TAD formation by serving as boundary elements.[11] Deletions, inversions, or duplications occurring near specific TAD boundaries can cause developmental defects.[12,13] However, the intricate relationship between alterations in the 3D genome and ocular diseases remains not fully understood. One well-documented cohesinopathy is Cornelia de Lange syndrome (CdLS), characterized by multiple systemic developmental abnormalities, including ocular manifestations such as myopia, strabismus, blepharoptosis, nystagmus, and abnormal fundus presentations.[14–17]

Previously, we identified a RAD21 mutation associated with a congenital corneal opacity disease called sclerocornea.[18] The RAD21 mutation R450C led to enhanced expression of protocadherin clusters (PCDHs), especially PCDHGC3, and disrupted the migration of neural crest cells (NCCs) during *Xenopus* corneal development.[19] During embryonic eye formation, NCCs migrate into the space between the corneal epithelium and endothelium and differentiate into corneal keratocytes. The arrangement of corneal stromal fiber architecture in sclerocornea patients is similar to scleral stromal fibers.[20] As scleral stroma is also derived from NCCs, whether the aberrant migration of NCCs can cause sclerocornea is unknown. Therefore, in this study we explored the roles and mechanisms of *RAD21* in regulating the differentiation fate determination and migration of NCCs with human embryonic stem cell (hESC)-derived NCCs and *Xenopus* embryos.

[1]Shandong First Medical University and Shandong Academy of Medical Sciences, Jinan, Shandong, China
[2]Eye Institute of Shandong First Medical University, Qingdao Eye Hospital of Shandong First Medical University, Qingdao, China
[3]School of Ophthalmology, Shandong First Medical University, Qingdao, China
[4]State Key Laboratory Cultivation Base, Shandong Provincial Key Laboratory of Ophthalmology, Qingdao, China
[5]Department of Chemical Biology, School of Life Sciences, Guangdong Provincial Key Laboratory of Cell Microenvironment and Disease Research, Shenzhen Key Laboratory of Cell Microenvironment, Southern University of Science and Technology, Shenzhen, China
[6]Department of Ophthalmology and Visual Sciences, The Chinese University of Hong Kong, Hong Kong, China
[7]Lead contact
*Correspondence: zbnxtt@gmail.com
https://doi.org/10.1016/j.isci.2024.109875

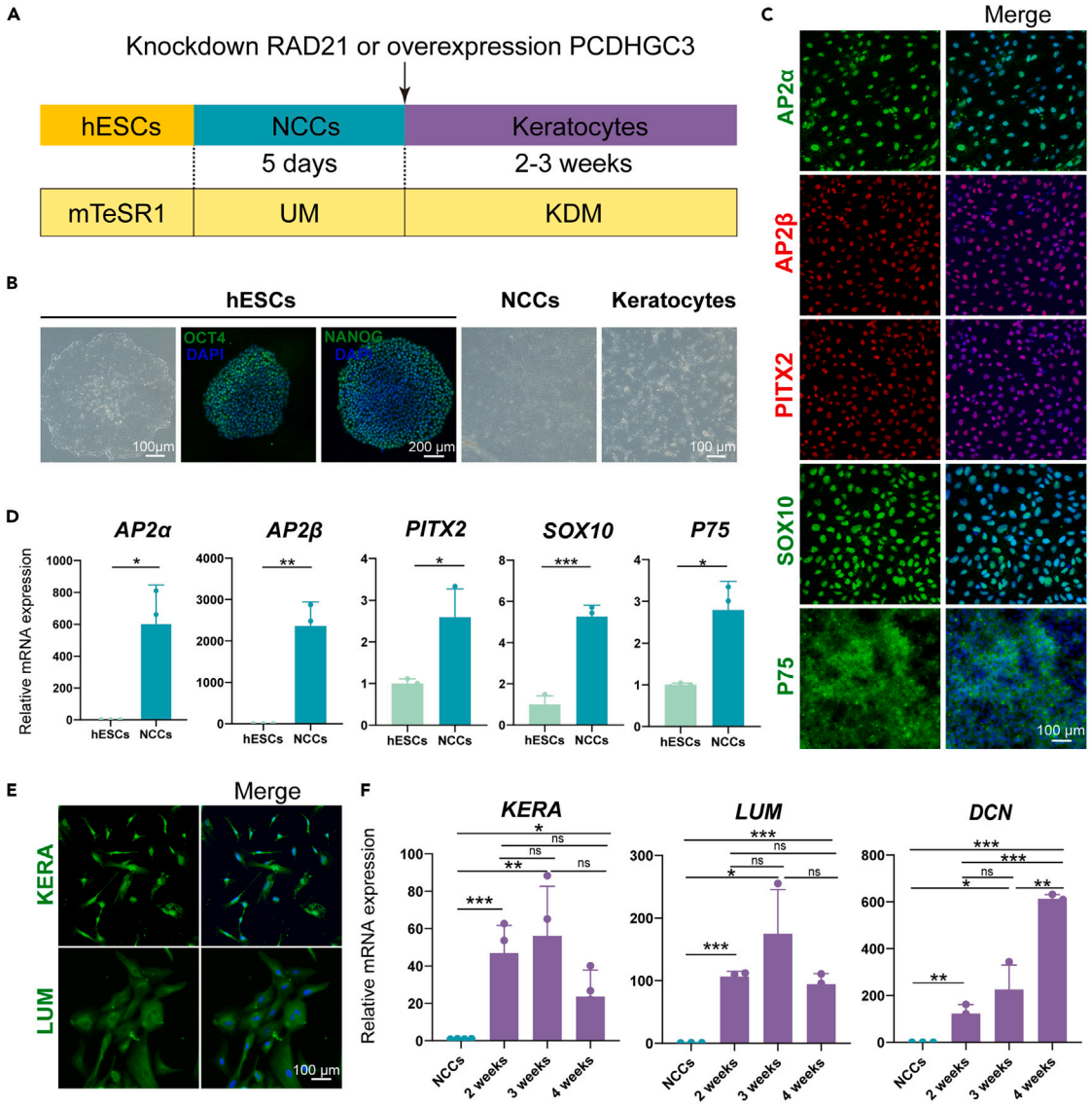

Figure 1. Differentiation of corneal keratocytes from hESCs

(A) Schematic representation of the methodology employed to induce the differentiation of hESCs into NCCs and subsequently into corneal keratocytes. NCCs were generated by incubating hESCs in NDM supplemented with 4 ng/mL bFGF and 1 μM RA for 5 days. To differentiate into keratocytes, the medium was switched to KDM containing 10 ng/mL bFGF for 2–3 weeks.

(B) Fluorescence microscopy images depicting hESCs, NCCs, and keratocytes. Scale bar = 100 μm. The immunostaining staining of pluripotency markers OCT4 and NANOG in hESCs showed positive. Nuclei were counterstained with DAPI. Scale bar = 200 μm.

(C) Representative immunofluorescence staining showing the expression of NCC markers, including P75, PITX2, AP2β, and SOX10. Nuclei were counterstained with DAPI. Scale bar = 100 μm.

(D) qPCR analysis of gene expression of NCC markers. $n = 3$.

(E) Representative immunofluorescence staining of keratocyte markers KERA and LUM. Nuclei were counterstained with DAPI. Scale bar = 100 μm.

(F) qPCR analysis of gene expression of keratocyte markers. $n = 3$. Data are presented as mean ± standard deviation. $^{*}p < 0.05$, $^{**}p < 0.01$, $^{***}p < 0.001$, ns, no significance.

RESULTS

Establishment of a differentiation pipeline for hESC-derived corneal keratocytes

We employed a two-step differentiation strategy to replicate the *in vivo* differentiation process, first differentiating hESCs into NCCs, followed by the differentiation of NCCs into keratocytes (Figure 1A). The hESC colonies exhibited clear boundaries and dense packaging, confirmed by positive immunostaining for pluripotency markers OCT4 and NANOG (Figure 1B). After 5 days of differentiation, there was a significant decrease in the gene expression of *OCT4* and *NANOG* (Figure S1A). The induced NCCs displayed polygonal shapes, increased cellular volume, and a

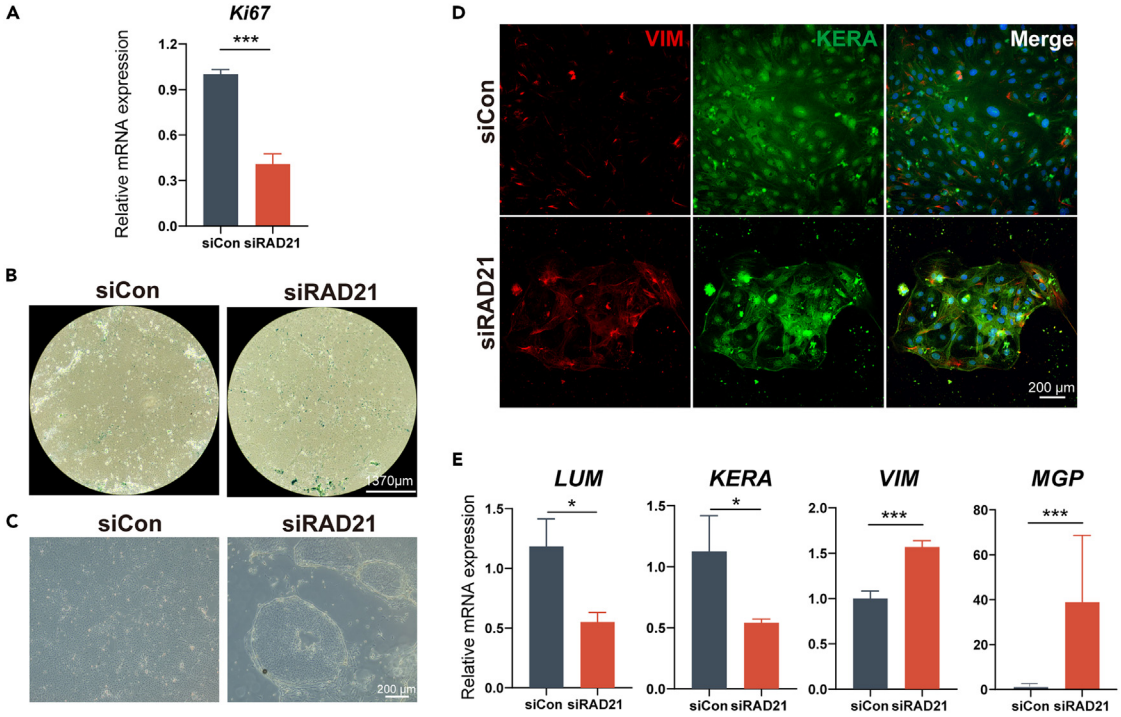

Figure 2. Impact of RAD21 deficiency on NCC activity

(A) *Ki67* exhibited 0.4-fold lower in the siRAD21 group compared to the siCon group. $n = 3$.

(B) During the NCC differentiation process, SA-β-Gal staining revealed enhanced senescence features in NCCs with RAD21 deficiency. Scale bar = 1370 μm. $n = 3$.

(C) During NCC differentiation into keratocytes, RAD21 knockdown cells exhibited clustering. Scale bar = 200 μm. $n = 3$.

(D) Immunofluorescence staining at the end of differentiation revealed lower expression of KERA in the siRAD21 group compared to the siCon group, while VIM was more enriched in the siRAD21 group than in the siCon group. The siRAD21 group displayed reduced cell numbers and clustered growth. Scale bar = 200 μm.

(E) qPCR displayed consistent expression trends for *KERA* and *VIM* as observed in (D). The scleral marker *MGP* exhibited 38.9-fold higher in the siRAD21 group compared to the siCon group according to RNA sequencing data. Data are presented as mean ± standard deviation. $n = 3$. *$p < 0.05$, ***$p < 0.001$.

reduced nuclear-cytoplasmic ratio, all of which are consistent to reported NCC characteristics (Figure 1B). The significant upregulation of neural crest markers AP2α, AP2β, PIXT2, SOX10, and P75 confirmed the successful induction of NCCs (Figures 1C and 1D), and all of which were absent or in low abundance in hESCs or keratocytes (Figures S1B and S1C).[21–23] Following the establishment of stable NCC colonies, we initiated the second phase of differentiation, and keratocytes were presented after 2–3 weeks of induction (Figure 1A). These keratocytes exhibited a spindle-shaped morphology (Figure 1B) and tested positive for keratocyte markers KERA and LUM (Figure 1E). Both qPCR (quantitative real-time PCR) and WB (Western blot) confirmed the significant upregulation of corneal stromal markers KERA, LUM, and DCN (Figures 1F and S1D). In conclusion, our two-step differentiation approach reliably generates NCCs and keratocytes from hESCs.

RAD21 depletion impairs NCC proliferation and differentiation

To assess the impact of RAD21 loss-of-function on NCC activities, we employed an RNA interference strategy to knock down *RAD21* during the differentiation of hESCs to NCCs. The knockdown group (siRAD21) exhibited a 29% reduction in *RAD21*, while a control sequence (siCon) had no effect on *RAD21* expression (Figure S2A). Correspondingly, RAD21 protein levels were notably diminished, with a decrease of 32.5% for the 130 kDa full-length RAD21 and 34.8% for the 75 kDa cleaved RAD21, respectively (Figures 2B and 2C). Knock down of *RAD21* showed no obvious influence on hESCs differentiation into NCCs (Figure S3). siRAD21-treated NCCs exhibited a significant decrease in *Ki67* expression (Figure 2A), indicating reduced cellular proliferation. Additionally, an elevation in senescence was observed in the siRAD21 group through SA-β-gal staining (Figure 2B). siRAD21-treated NCCs tended to form round clusters during differentiation into keratocytes (Figure 2C), and these aggregated cells exhibited more pronounced vimentin (VIM) staining (Figure 2D). qPCR analysis revealed a significant 3.6-fold increase in *VIM* and 38.9-fold increase in matrix Gla (*MGP*), both of which are markers of scleral stroma,[24,25] accompanied by reduced levels of corneal stroma *LUM* and *KERA* expression (Figure 2E).

Upregulation of PCDHGC3 in RAD21 deficient cells affects NCC activities

We further investigated the underlying mechanisms of the impact of RAD21 posed on NCCs. RAD21 is a cohesion complex subunit and works with CTCF to regulate gene expression by forming promoter-enhancer loops. Previously we identified the *PCDHGC3* being as the top

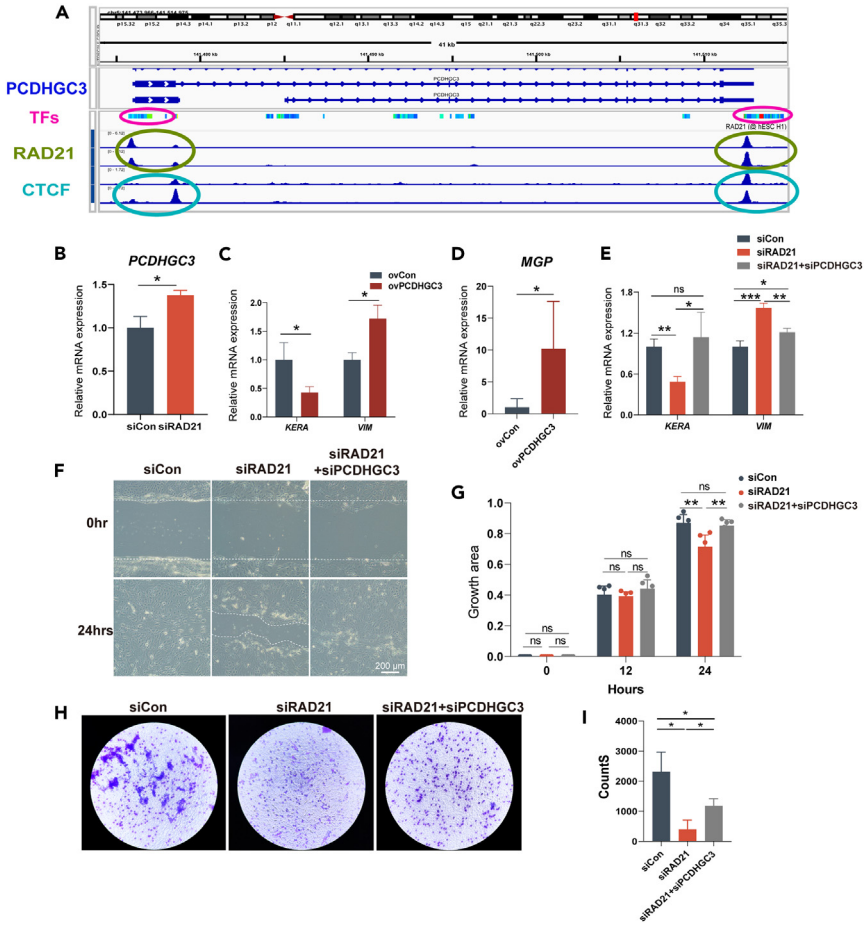

Figure 3. RAD21 induced upregulation of *PCDHGC3*

(A) Peaks of RAD21 (green circles), CTCF (blue circles), and TFs (red circles) are observed in both upstream and downstream of the *PCDHGC3* gene.

(B) qPCR analysis revealed upregulated *PCDHGC3* expression in siRAD21-treated NCCs. *PCDHGC3* exhibited 1.4-fold higher in the siRAD21 group than in the siCon group. $n = 3$.

(C) At the end of differentiation, *KERA* exhibited 0.4-fold lower and *VIM* exhibited 1.7-fold higher in the ovPCDHGC3 group compared to the ovCon group. $n = 3$.

(D) The scleral marker *MGP* exhibited 10.2-fold higher in the ovPCDHGC3 group compared to the ovCon group according to RNA sequencing data. $n = 3$.

(E) Knock down of *PCDHGC3* in RAD21-deficient NCCs served as a rescue strategy, and restored gene expression in *KERA* and *VIM*. $n = 3$.

(F) Time-lapse images at time 0 and 24 h post-scratching. Scale bar = 200 μm.

(G) Quantitative analysis of (F). At 24 h, the wound healing area of the rescue group was 1.2-fold higher than that of the siRAD21 group, resembling that of the siCon group. $n = 3$.

(H) The transwell assay detects cell migration.

(I) Quantitative analysis of (H). The number of migratory cells in the rescue group was 2.9-fold higher than in the siRAD21 group. Data are presented as mean ± standard deviation. $n = 3$. $^{*}p < 0.05$, $^{**}p < 0.01$, $^{***}p < 0.001$, ns, no significance.

upregulated gene together with local chromosomal structural changes in primary lymphoblastoid cells of sclerocornea patients.[19] Here we validated the observation by searching the Cistrome Data Browser database.[26,27] Indeed, peaks of RAD21, CTCF, and transcription factors (TFs) are observed in both upstream and downstream of the *PCDHGC3* gene (Figure 3A). In siRAD21-treated NCCs, *PCDHGC3* was also significantly upregulated (Figure 3B), and overexpressing *PCDHGC3* in NCCs through plasmid transfection (ovPCDHGC3) led to decline in *KERA* and upregulation of *VIM* (Figure 3C) and *MGP* (Figure 3D). We performed a rescue assay by co-knockdown of *RAD21* and *PCDHGC3*. Interestingly, double restored *KERA* expression and suppressed *VIM* expression (Figure 3E).

We also examined NCC migration by scratch assay and transwell assay. siRAD21 NCCs displayed obvious delay in scratch wound healing (Figures 3F and 3G) and significantly decreased transwell cell counts (Figures 3H and 3I), while double knock down of *RAD21* and *PCDHGC3* rescued the migration in both experiments (Figures 3F–3I). Collectively, these findings suggested a downstream role of *PCDHGC3* in *RAD21* influencing NCC activities.

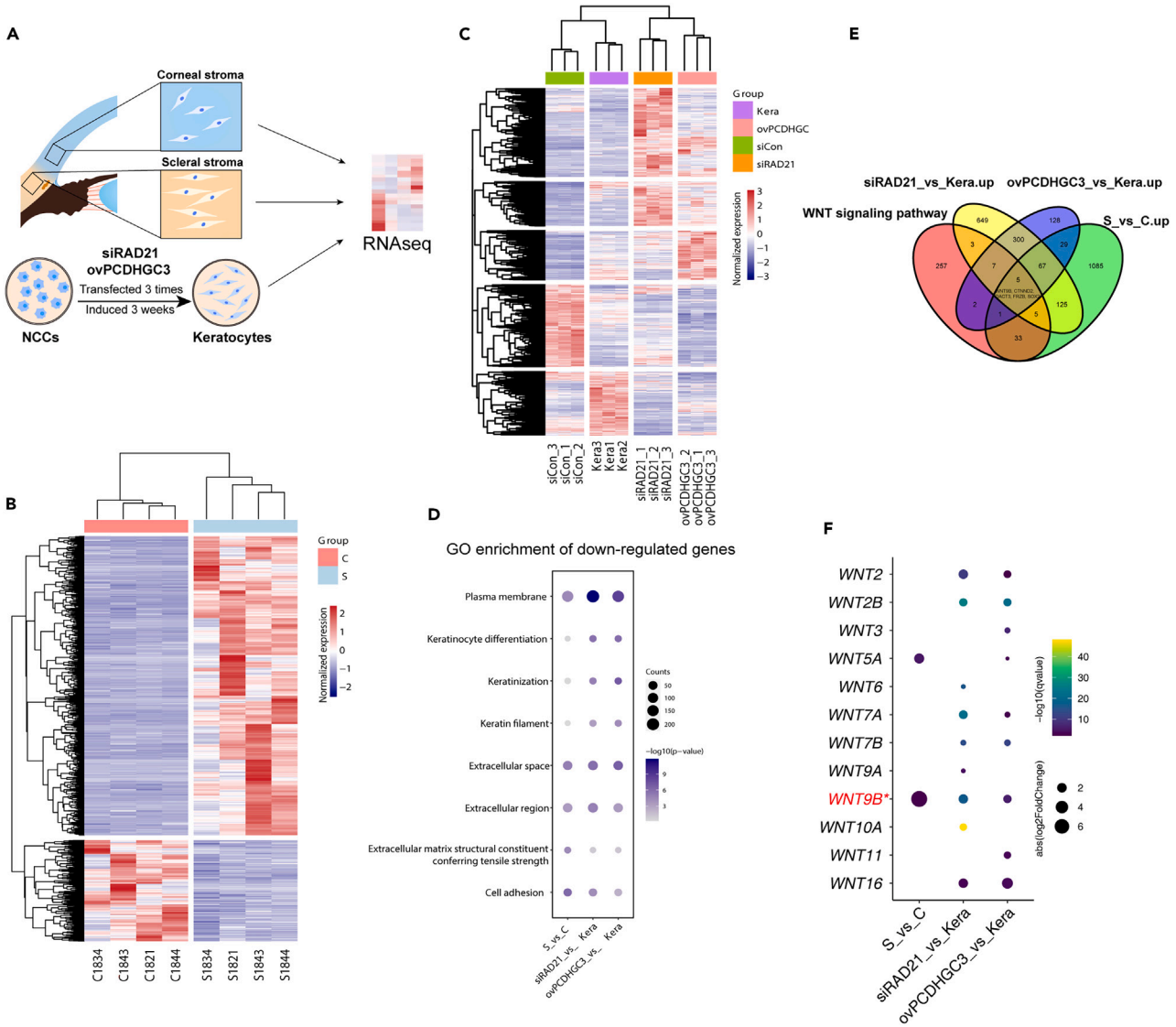

Figure 4. Transcriptome analysis

(A) Transcriptome sequencing sample schematic. Four human corneal stroma samples (group C), four human scleral stroma samples (group S), and NCCs with RAD21 knockdown (siRAD21) or NCCs with PCDHGC3 overexpression (ovPCDHGC3) were also sequenced.

(B) Hierarchical clustering heatmap of differentially expressed genes in different samples (S and C).

(C) Hierarchical clustering heatmap of differentially expressed genes in different samples (siRAD21, ovPCDHGC3, Kera, and siCon).

(D) Top GO terms for commonly downregulated genes in siRAD21 vs. Kera, ovPCDHGC3 vs. Kera, and S vs. C conditions.

(E) A Venn diagram illustrated the common upregulated genes in siRAD21 vs. Kera, ovPCDHGC3 vs. Kera, and S vs. C conditions with canonical WNT signaling pathway genes.

(F) Bubble map of the WNT gene family illustrated genes with significant differences common to siRAD21 vs. Kera, ovPCDHGC3 vs. Kera, and S vs. C.

WNT9B drives scleral commitment of NCCs

To further determine the regulatory mechanism of NCC commitment, we performed RNA sequencing with four human corneal stroma samples (group C) and four human scleral stroma samples (group S) (Figure 4A). Corneal stroma and scleral stroma displayed distinctive separation in expression profiles (Figure 4B). Gene ontology (GO) analysis showed that genes preferentially expressed in the scleral stroma are "extracellular matrix organization," "muscle system process," and "mesenchyme development" (Figure S4A), while "cell junction assembly," "regulation of axonogenesis," and "cell-substrate adhesion" were more enriched in the corneal stroma (Figure S4B). NCCs with RAD21 knockdown (siRAD21) or NCCs with PCDHGC3 overexpression (ovPCDHGC3) were also sequenced (Figure 4A). According to the hierarchical clustering heatmaps of differentially expressed genes (DEGs), siRAD21 group similar expression profile to ovPCDHGC3 group, while the

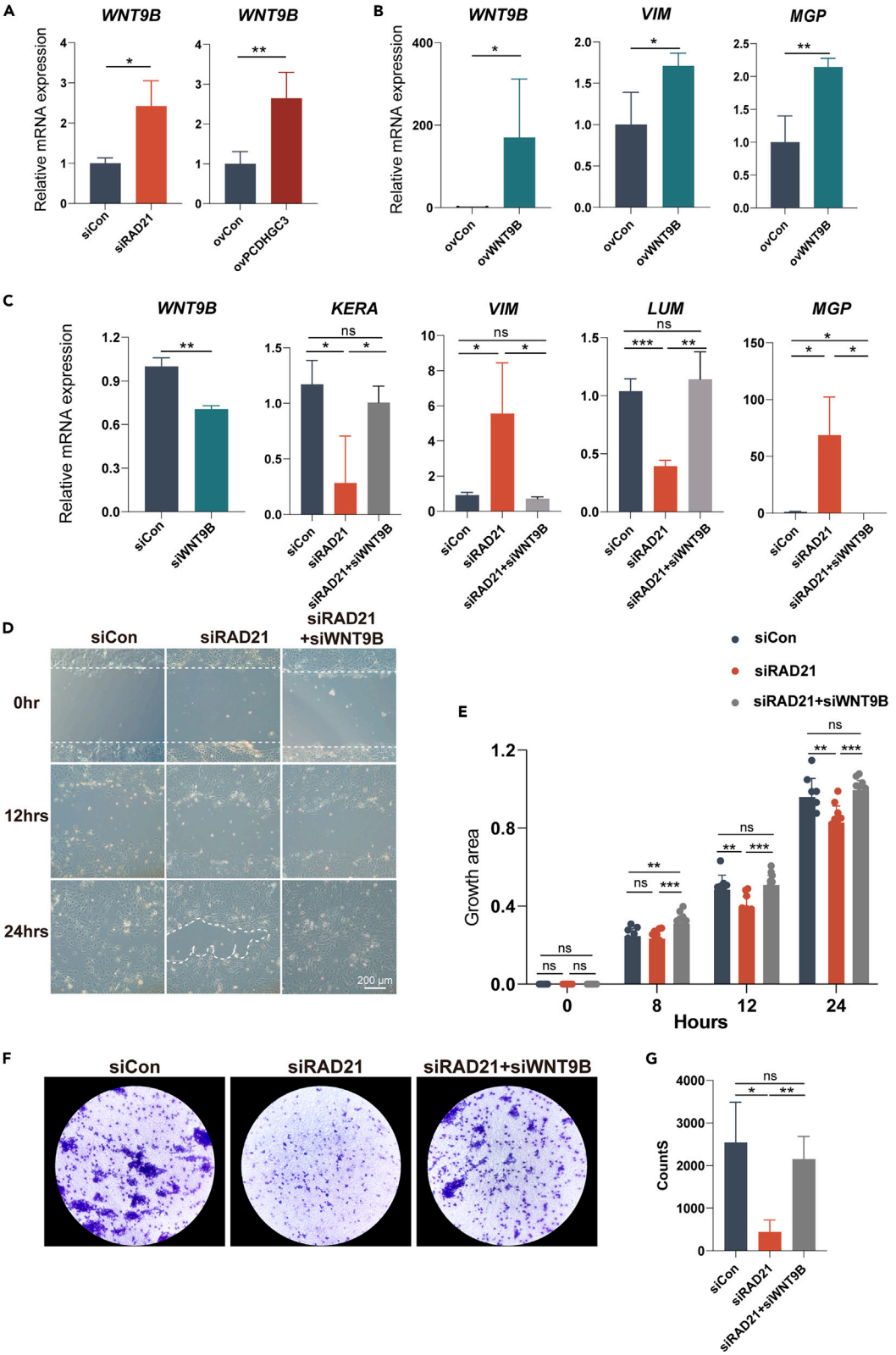
A
WNT9B
WNT9B
Relative mRNA expression
siCon
siRAD21
ovCon
ovPCDHGC3
B
WNT9B
VIM
MGP
Relative mRNA expression
ovCon
ovWNT9B
C
WNT9B
KERA
VIM
LUM
MGP
Relative mRNA expression
siCon
siWNT9B
siRAD21
siRAD21+siWNT9B
D
siCon
siRAD21
siRAD21
+siWNT9B
0hr
12hrs
24hrs
200 μm
E
siCon
siRAD21
siRAD21+siWNT9B
Growth area
Hours
F
siCon
siRAD21
siRAD21+siWNT9B
G
CountS
siCon
siRAD21
siRAD21+siWNT9B

Figure 5. Knock down of *WNT9B* rescues defects in RAD21

(A) *WNT9B* exhibited 2.4-fold higher in the siRAD21 group compared to the siCon group and 2.6-fold higher in the ovPCDHGC3 group compared to the ovCon group. $n = 3$.

(B) qPCR analysis of the efficiency of overexpression of *WNT9B* in NCCs. $n = 3$. At the end of differentiation, *VIM* and *MGP* exhibited 1.7-fold and 2.1-fold higher in the ovWNT9B group compared to the ovCon group. $n = 3$.

(C) Knock down of *WNT9B* in RAD21-deficient NCCs served as a rescue strategy, and restored gene expression in *KERA*, *VIM*, *LUM*, and *MGP*. $n = 3$.

(D) Time-lapse images at time 0, 12, and 24 h post-scratching. Scale bar = 200 μm.

(E) Quantitative analysis of (D). At 12 h and 24 h, the wound healing area of the rescue group was 1.3-fold higher and 1.2-fold higher compared to the siRAD21 group, resembling that of the siCon group. $n = 3$.

(F) The transwell assay detects cell migration.

(G) Quantitative analysis of (F). The number of migratory cells in the rescue group was 4.9-fold higher than in the siRAD21 group and being 0.8-fold of the siCon group. Data are presented as mean ± standard deviation. $n = 3$. $^{*}p < 0.05$, $^{**}p < 0.01$, $^{***}p < 0.001$, ns, no significance.

keratocytes differentiated from NCCs transfected with siCon (Group siCon) was closer to standard keratocytes differentiated from wild-type NCCs (group Kera) (Figure 4C).

We then analyzed the overlapping downstream factors shared the scleral prone groups (group S, siRAD21, and ovPCDHGC3). Their shared terms were like keratinocyte differentiation, keratinization, extracellular space, and cell adhesion (Figure 4D). WNT signaling pathway is a critical and classical pathway in regulating corneal stromal development.[28,29] NCC proliferation is dependent on WNT signaling in both mice[30] and zebrafish.[31] Therefore, we performed a combined analysis for the WNT pathway and our RNA sequencing data, and identified five shared candidate genes including *WNT9B*, *CTNND2*, *DACT3*, *FRZB*, and *SOX2* (Figure 4E). In addition, among all the WNT members examined, *WNT9B* was the most differentiated gene in these three groups (Figure 4F), which was 190.9-fold higher in group S compared to group C, 3.8-fold higher in group siRAD21 compared to group Kera, and 2.6-fold higher in group ovPCDHGC3 compared to group Kera. *In vitro* validation also revealed upregulation *WNT9B* by 2.4-fold in siRAD21 NCCs and 2.6-fold in ovPCDHGC3 NCCs (Figure 5A).

To confirm that *WNT9B* is a downstream regulator of *RAD21*, we first examined the chromatin architecture surrounding *WNT9B*. As was expected, enriched CTCF and RAD21 peaks were observed before and after *WNT9B* (Figure S5).[26,27] Additionally, we overexpressed *WNT9B* in NCCs through plasmid transfection (ovWNT9B). The ovWNT9B cells exhibited an upregulation of *VIM* and *MGP* (Figure 5B), a trend like NCCs treated with siRAD21 (Figure 2E) and ovPCDHGC3 (Figure 3C). Double knockdown by co-transfecting siWNT9B and siRAD21 restored the expression of differentiation markers (Figure 5C). Additionally, this rescue strategy effectively rescued the migration of NCCs in the scratch assay (Figures 5D and 5E) and the transwell assay (Figures 5F and 5G). All of these findings indicated the downstream regulatory role of *WNT9B* in NCCs, and the essential function of *WNT9B* in NCC differentiation and migration.

Overexpression of *wnt9b* lead to abnormities in *X. tropicalis* cranical NCCs migration and eye development

In wild-type *X.tropicalis* embryos, *wnt9b* was initially detected at stage 22 in the surface ectoderm of the branchial arches and remained within this area till stage 28.[32] By stage 28, *wnt9b* expression became more prominent in the eye and overlapped with the expression of NCC markers *ap2a* and *twist1*, indicating a potential connection between *wnt9b* and NCC activity (Figure S6).

As WNT9B was upregulated in scleral-prone NCCs, to examine the harmful role of *wnt9b* on cranial NCCs *in vivo*, we microinjected *wnt9b* mRNA into one cell of two-cell stage embryos (ovWNT9B). At stage 28, *in situ* hybridization for *ap2α* and *twist1* showed that on the embryonic side with ovWNT9B, 75% (38/51) of embryos displayed disrupted NCC migration patterns, with indistinct migration streams around the optic cup (oc) and at the three branchial arches (ba) (Figure 6A), significantly higher than the developmental defects observed in the non-injected side (17.6%, 9/51) (Figure 6A). Similarly, *twist1* staining demonstrated 78% (38/49) disrupted NCC pattern in ovWNT9B side, compared to 10.2% (5/49) in the control side (Figure 6B). Both markers demonstrated significant difference (Figure 6C). We further followed the migration of periocular mesenchyme (POM) in later developmental stages. The stage 41 *X. tropicalis* eyes were collected and stained with *pitx2* to visualize POM (Figure 6D). The purple staining intensity on the ovWNT9B side was significantly weaker, which was only 38% of that in the non-injected eye of the same embryo (Figure 6E), indicating a lack of POM within corneal stromal region upon *wnt9b* overexpression.

To avoid the ocular abnormities caused by mRNA injection, we applied GFP mRNA as control, and *wnt9b* also fused with GFP. No visible defect can be observed till stage 41 in embryos microinjected with GFP at stage 2 (Figure 7A), whereas 90% (9/10) of eyes with *wnt9b* overexpression were malformed (Figure 7B). These eyes showed an incomplete iris development, shortened interocular distance (semi-fusion), and abnormal lens morphology (Figure S7). In conclusion, RAD21 deficiency can lead to improper overexpression of *wnt9b*, and therefore affects NCC migration into the eye, and causes abnormal ocular development.

DISCUSSION

Cases of sclerocornea have been associated with a point mutation in the cohesion subunit RAD21. In this study, knock down of *RAD21* or overexpression of the downstream gene *PCDHGC3* in hESCs-derived NCCs disrupted cell migration and altered cell fate during differentiation. Transcriptomic analysis revealed differential expression of *WNT9B* in the WNT signaling pathway. In *X. tropicalis* overexpression of *wnt9b* resulted in abnormal migration of cranial NCCs. Our findings suggest that *RAD21* mutation can influence eye development via regulating the expression of some developmental essential genes, such as *PCDHGC3* and *WNT9B*.

In previous research, we demonstrated that the *RAD21* mutation influences the entire PCDHGC gene cluster. This cluster has shared regulatory mechanisms, including promoters and enhancers. While *PCDHGC3* showed the most significant differential expression within this

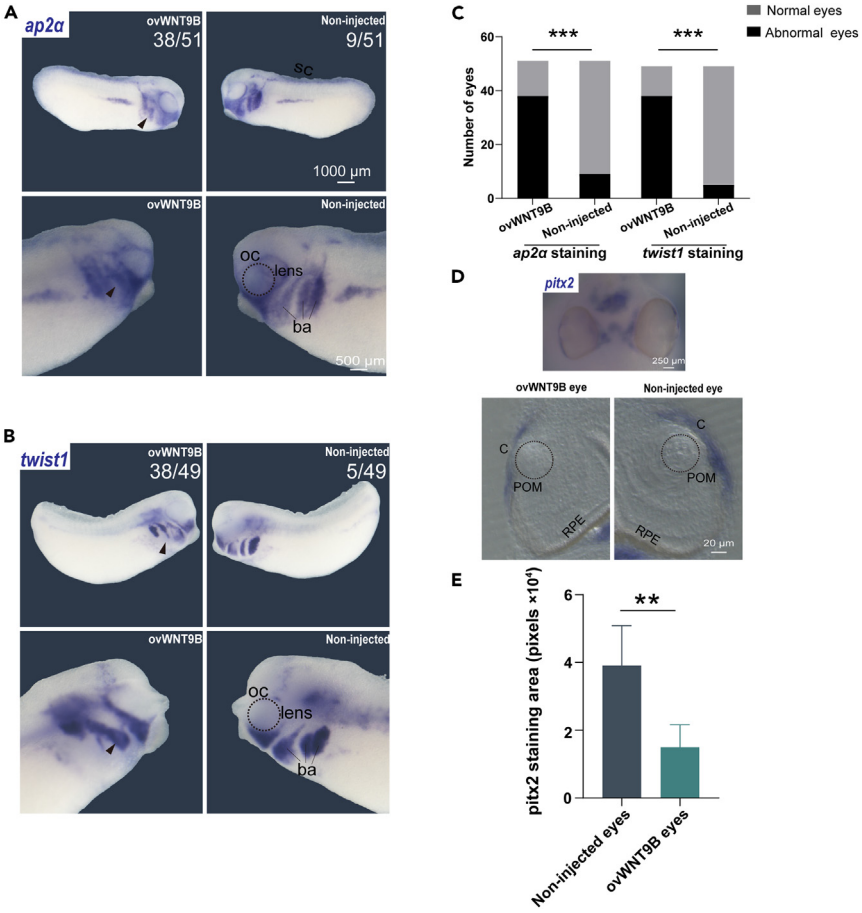

Figure 6. ovWNT9B affected NCCs Migration in *X. tropicalis*

(A) At stage 28, the *in situ* hybridization pattern of ap2a on the non-injected side of the same embryo shows intact and clear NCC migration around the oc and three ba. In contrast, on the ovWNT9B side, these structures are disrupted (38/51). Scale bar upper panel = 1000 μm, lower panel = 500 μm.

(B) At stage 28, the *in situ* hybridization pattern of twist1 on the non-injected side of the same embryo shows intact and clear NCC migration around the oc and three ba, while on the ovWNT9B side a delayed NCC migration was observed (38/49). Scale bar upper panel = 1000 μm, lower panel = 500 μm.

(C) Number of embryos with normal and abnormal NCC migration in each group.

(D) The *in situ* hybridization of pitx2 at stage 41. Both the ovWNT9B eye and the non-injected eye, as well as their ocular sections, were shown. $n = 5$. Scale bar upper panel = 250 μm, lower panel = 20 μm.

(E) Quantitative analysis of the pitx2-positive area in the POM of non-injected eyes and eyes with wnt9b overexpression. Data are presented as mean ± standard deviation. $n = 5$. $^{**}p < 0.01$. $^{***}p < 0.001$.

cluster,[19] we acknowledge the potential roles of other members. Another group reported the impact of chromosomal structure changes on *PCDHGC3* expression during corneal epithelial development,[17] indicating our observations were not isolated. In this study, we confirmed that *RAD21* knockdown upregulated *PCDHGC3*, and knock down of *PCDHGC3* rescued phenotypes associated with *RAD21* deficiency, suggesting a potential interaction between *RAD21* and *PCDHGC3*.

The corneal stroma originates from NCCs, and disruption of NCC migration during corneal development can lead to congenital corneal opacity. In our previous study, *in situ* hybridization of *rad21* in *Xenopus laevis* revealed enrichment around the eye at stage 39.[20] However, in this study, we constructed the *Xenopus* model by microinjection of *wnt9b* into the embryo at the 2-cell stage, inducing earlier gene expression changes and potentially more severe phenotypes. Indeed, overexpression of *wnt9b* resulted in a spectrum of ocular abnormalities more severe than sclerocornea-like phenotypes. We selectively overexpressed *wnt9b* in one cell of the *Xenopus* embryo, while leaving the other cell non-injected, serving as a control. However, *in situ* hybridization of NCC markers *ap2α* and *twist1* revealed disruptions in NCC migration in 17.6% and 10.2% of eyes on the control side as well, possibly due to the interdependence of these two eyes during amphibian embryonic development. They influence each other through intercellular signaling molecules and cell-cell interactions, leading to developmental abnormalities on the non-injected side in some embryos.

Both corneal and scleral tissues originate from NCCs but undergo differentiation under distinct regulatory environments and at different developmental stages.[33,34] During week 6.4 of human embryonic development, periocular NCCs initiate differentiation into

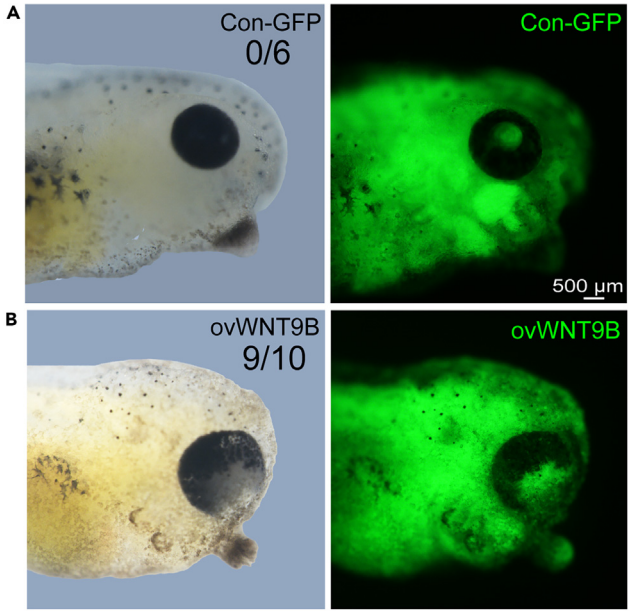

Figure 7. ovWNT9b affected eye development

(A) At the two-cell stage of embryonic development, GFP was injected into one cell. At stage 41, there was no obvious abnormality in eye morphology developed from the injected cell. Scale bar = 500 μm.

(B) At the two-cell stage of embryonic development, a combination of *wnt9b* and GFP was injected into one cell. At stage 41, 90% of eyes with *wnt9b* overexpression were malformed. Scale bar = 500 μm.

fibroblasts. By week 7, NCCs contribute to the formation of the corneal stroma, while scleral stroma formation begins around week 7.2.[34] Limited information exists regarding scleral development, although studies suggest its potential association with factors such as retinoic acid (RA) and basic fibroblast growth factor (bFGF) secreted by the choroid.[35,36] Corneal development is governed by a complex interplay of factors such as the WNT/β-catenin pathway, FGF, RA, TGF-β signaling pathway, along with TFs *PAX6*, *FOXC1*, and *PITX2*.[28,37–39] For instance, *TGF-β2* knockout mice exhibited corneal stromal thinning and reduced expression of corneal stromal markers *Kera* and *Lum*.[40] Disruption of NCCs has been noted in *Foxc1* mutant mice.[37] In human, the WNT family comprises 19 members. While studies in zebrafish have demonstrated the regulation of NCC fate by *Wnt1* and *Wnt3a*,[31] research on *WNT9B* remains scarce. A study tracking the expression of *Wnt9b* through whole-mount *in situ* hybridization (WISH) in chicken demonstrated its role in regulating the morphogenesis of corneal epithelium.[41] In mice, spatiotemporal expression patterns of *Wnt9b* and its downstream *TOPGAL* were examined in wild-type mice and *Wnt9b* mutant mice, revealing that *Wnt9B* regulates lip fusion.[42] In this study, we identified *WNT9B* as a shared upregulated downstream gene following either *RAD21* knockdown or *PCDHGC3* overexpression. Consistently, knock down of *WNT9B* in NCCs rescued the differentiation and migration abnormalities caused by *RAD21* knockdown, highlighting its crucial role in cell fate determination during corneal development.

Limitations of the study

Our choice of WNT9B as a target may be limited. WNT is the key regulatory pathway during corneal development. While only a few genes overlapped in our study, our selected target demonstrated good specificity. Both the treatment (overexpression of WNT9B) and rescue (knockdown WNT9B) showed significant outcomes compared to their controls. But still, the roles of other pathways or genes cannot be excluded, as they may also play important roles in corneal development or sclerocornea pathogenesis.

STAR★METHODS

Detailed methods are provided in the online version of this paper and include the following:

- KEY RESOURCES TABLE
- RESOURCE AVAILABILITY
  - Lead contact
  - Materials availability
  - Data and code availability
- EXPERIMENTAL MODEL AND STUDY PARTICIPANT DETAILS

SUPPLEMENTAL INFORMATION

Supplemental information can be found online at https://doi.org/10.1016/j.isci.2024.109875.

ACKNOWLEDGMENTS

We are grateful to Professor Yin Zhengqin of the Southwest Hospital/Southwest Eye Hospital, Army Medical University, for generously providing the human embryonic stem cell line H1. This study was supported by the National Natural Science Foundation of China (82101091 to B.N.Z.) and the Shandong Provincial Natural Science Foundation (ZR2020QH140 to B.N.Z.).

AUTHOR CONTRIBUTIONS

Conceptualization, B.N.Z., Q.Z., Y.C., and Z.L.; methodology, H.L., B.Q., G.L., H.D., and Z.S.; formal analysis, H.L. and B.Q.; investigation, H.L. and B.N.Z.; resources, B.N.Z., Y.C., and Z.L.; writing, H.L., W.K.C., and B.N.Z.; funding acquisition, B.N.Z.

DECLARATION OF INTERESTS

The authors declare no competing interests.

Received: November 2, 2023
Revised: February 28, 2024
Accepted: April 29, 2024
Published: May 3, 2024

REFERENCES

1. Levine, M., and Tjian, R. (2003). Transcription regulation and animal diversity. Nature *424*, 147–151. https://doi.org/10.1038/nature01763.
2. Sexton, T., and Cavalli, G. (2015). The role of chromosome domains in shaping the functional genome. Cell *160*, 1049–1059. https://doi.org/10.1016/j.cell.2015.02.040.
3. Gorkin, D.U., Leung, D., and Ren, B. (2014). The 3D genome in transcriptional regulation and pluripotency. Cell Stem Cell *14*, 762–775. https://doi.org/10.1016/j.stem.2014.05.017.
4. Andrey, G., and Mundlos, S. (2017). The three-dimensional genome: regulating gene expression during pluripotency and development. Development *144*, 3646–3658. https://doi.org/10.1242/dev.148304.
5. Peters, J.M., Tedeschi, A., and Schmitz, J. (2008). The cohesin complex and its roles in chromosome biology. Genes Dev. *22*, 3089–3114. https://doi.org/10.1101/gad.1724308.
6. Phillips-Cremins, J.E., Sauria, M.E.G., Sanyal, A., Gerasimova, T.I., Lajoie, B.R., Bell, J.S.K., Ong, C.T., Hookway, T.A., Guo, C., Sun, Y., et al. (2013). Architectural protein subclasses shape 3D organization of genomes during lineage commitment. Cell *153*, 1281–1295. https://doi.org/10.1016/j.cell.2013.04.053.
7. Kagey, M.H., Newman, J.J., Bilodeau, S., Zhan, Y., Orlando, D.A., van Berkum, N.L., Ebmeier, C.C., Goossens, J., Rahl, P.B., Levine, S.S., et al. (2010). Mediator and cohesin connect gene expression and chromatin architecture. Nature *467*, 430–435. https://doi.org/10.1038/nature09380.
8. Khaminets, A., Ronnen-Oron, T., Baldauf, M., Meier, E., and Jasper, H. (2020). Cohesin controls intestinal stem cell identity by maintaining association of Escargot with target promoters. Elife *9*, e48160. https://doi.org/10.7554/eLife.48160.
9. Dixon, J.R., Selvaraj, S., Yue, F., Kim, A., Li, Y., Shen, Y., Hu, M., Liu, J.S., and Ren, B. (2012). Topological domains in mammalian genomes identified by analysis of chromatin interactions. Nature *485*, 376–380. https://doi.org/10.1038/nature11082.
10. Nora, E.P., Goloborodko, A., Valton, A.L., Gibcus, J.H., Uebersohn, A., Abdennur, N., Dekker, J., Mirny, L.A., and Bruneau, B.G. (2017). Targeted Degradation of CTCF Decouples Local Insulation of Chromosome Domains from Genomic Compartmentalization. Cell *169*, 930–944.e22. https://doi.org/10.1016/j.cell.2017.05.004.

11. Merkenschlager, M., and Nora, E.P. (2016). CTCF and Cohesin in Genome Folding and Transcriptional Gene Regulation. Annu. Rev. Genomics Hum. Genet. *17*, 17–43. https://doi.org/10.1146/annurev-genom-083115-022339.
12. Lupiáñez, D.G., Kraft, K., Heinrich, V., Krawitz, P., Brancati, F., Klopocki, E., Horn, D., Kayserili, H., Opitz, J.M., Laxova, R., et al. (2015). Disruptions of topological chromatin domains cause pathogenic rewiring of gene-enhancer interactions. Cell *161*, 1012–1025. https://doi.org/10.1016/j.cell.2015.04.004.
13. Giorgio, E., Robyr, D., Spielmann, M., Ferrero, E., Di Gregorio, E., Imperiale, D., Vaula, G., Stamoulis, G., Santoni, F., Atzori, C., et al. (2015). A large genomic deletion leads to enhancer adoption by the lamin B1 gene: a second path to autosomal dominant adult-onset demyelinating leukodystrophy (ADLD). Hum. Mol. Genet. *24*, 3143–3154. https://doi.org/10.1093/hmg/ddv065.
14. Liu, J., and Krantz, I.D. (2009). Cornelia de Lange syndrome, cohesin, and beyond. Clin. Genet. *76*, 303–314. https://doi.org/10.1111/j.1399-0004.2009.01271.x.
15. Kline, A.D., Moss, J.F., Selicorni, A., Bisgaard, A.M., Deardorff, M.A., Gillett, P.M., Ishman, S.L., Kerr, L.M., Levin, A.V., Mulder, P.A., et al. (2018). Diagnosis and management of Cornelia de Lange syndrome: first international consensus statement. Nat. Rev. Genet. *19*, 649–666. https://doi.org/10.1038/s41576-018-0031-0.
16. Milot, J., and Demay, F. (1972). Ocular anomalies in de Lange syndrome. Am. J. Ophthalmol. *74*, 394–399. https://doi.org/10.1016/0002-9394(72)90897-5.
17. Li, M., Huang, H., Wang, B., Jiang, S., Guo, H., Zhu, L., Wu, S., Liu, J., Wang, L., Lan, X., et al. (2022). Comprehensive 3D epigenomic maps define limbal stem/progenitor cell function and identity. Nat. Commun. *13*, 1293. https://doi.org/10.1038/s41467-022-28966-6.
18. Zhang, B.N., Chan, T.C.Y., Tam, P.O.S., Liu, Y., Pang, C.P., Jhanji, V., Chen, L.J., and Chu, W.K. (2019). A Cohesin Subunit Variant Identified from a Peripheral Sclerocornea Pedigree. Dis. Markers *2019*, 8781524. https://doi.org/10.1155/2019/8781524.
19. Zhang, B.N., Liu, Y., Yang, Q., Leung, P.Y., Wang, C., Wong, T.C.B., Tham, C.C., Chan, S.O., Pang, C.P., Chen, L.J., et al. (2020). rad21 Is Involved in Corneal Stroma Development by Regulating Neural Crest Migration. Int. J. Mol. Sci. *21*, 7807. https://doi.org/10.3390/ijms21207807.
20. Zhang, B.N., Wong, T.C.B., Yip, Y.W.Y., Liu, Z., Wang, C., Wong, J.S.C., He, J.N., Chan, T.C.Y., Jhanji, V., Pang, C.P., et al. (2019). A sclerocornea-associated RAD21 variant induces corneal stroma disorganization. Exp. Eye Res. *185*, 107687. https://doi.org/10.1016/j.exer.2019.06.001.
21. Gong, Y., Duan, H., Wang, X., Zhao, C., Li, W., Dong, C., Li, Z., and Zhou, Q. (2021). Transplantation of human induced pluripotent stem cell-derived neural crest cells for corneal endothelial regeneration. Stem Cell Res. Ther. *12*, 214. https://doi.org/10.1186/s13287-021-02267-z.
22. Li, Z., Duan, H., Jia, Y., Zhao, C., Li, W., Wang, X., Gong, Y., Dong, C., Ma, B., Dou, S., et al. (2022). Long-term corneal recovery by simultaneous delivery of hPSC-derived corneal endothelial precursors and nicotinamide. J. Clin. Invest. *132*, e146658. https://doi.org/10.1172/jci146658.
23. Evans, A.L., and Gage, P.J. (2005). Expression of the homeobox gene Pitx2 in neural crest is required for optic stalk and ocular anterior segment development. Hum. Mol. Genet. *14*, 3347–3359. https://doi.org/10.1093/hmg/ddi365.
24. Sathiyanathan, P., Tay, C.Y., and Stanton, L.W. (2017). Transcriptome analysis for the identification of cellular markers related to trabecular meshwork differentiation. BMC Genom. *18*, 383. https://doi.org/10.1186/s12864-017-3758-7.
25. Tsai, C.L., Wu, P.C., Fini, M.E., and Shi, S. (2011). Identification of multipotent stem/progenitor cells in murine sclera. Invest. Ophthalmol. Vis. Sci. *52*, 5481–5487. https://doi.org/10.1167/iovs.11-7676.
26. Ji, X., Dadon, D.B., Powell, B.E., Fan, Z.P., Borges-Rivera, D., Shachar, S., Weintraub, A.S., Hnisz, D., Pegoraro, G., Lee, T.I., et al. (2016). 3D Chromosome Regulatory Landscape of Human Pluripotent Cells. Cell Stem Cell *18*, 262–275. https://doi.org/10.1016/j.stem.2015.11.007.
27. Xu, C., and Corces, V.G. (2018). Nascent DNA methylome mapping reveals inheritance of hemimethylation at CTCF/cohesin sites. Science *359*, 1166–1170. https://doi.org/10.1126/science.aan5480.
28. Ma, J., and Lwigale, P. (2019). Transformation of the Transcriptomic Profile of Mouse Periocular Mesenchyme During Formation of the Embryonic Cornea. Invest. Ophthalmol. Vis. Sci. *60*, 661–676. https://doi.org/10.1167/iovs.18-26018.
29. Bi, L., and Lwigale, P. (2019). Transcriptomic analysis of differential gene expression during chick periocular neural crest differentiation into corneal cells. Dev. Dyn. *248*, 583–602. https://doi.org/10.1002/dvdy.43.
30. Ikeya, M., Lee, S.M., Johnson, J.E., McMahon, A.P., and Takada, S. (1997). Wnt signalling required for expansion of neural crest and CNS progenitors. Nature *389*, 966–970. https://doi.org/10.1038/40146.
31. Dorsky, R.I., Moon, R.T., and Raible, D.W. (1998). Control of neural crest cell fate by the Wnt signalling pathway. Nature *396*, 370–373. https://doi.org/10.1038/24620.
32. Ito, Y.A., and Walter, M.A. (2014). Genomics and anterior segment dysgenesis: a review. Clin. Exp. Ophthalmol. *42*, 13–24. https://doi.org/10.1111/ceo.12152.
33. Eghrari, A.O., Riazuddin, S.A., and Gottsch, J.D. (2015). Overview of the Cornea: Structure, Function, and Development. Prog. Mol. Biol. Transl. Sci. *134*, 7–23. https://doi.org/10.1016/bs.pmbts.2015.04.001.
34. Sellheyer, K., and Spitznas, M. (1988). Development of the human sclera. A morphological study. Graefes Arch. Clin. Exp. Ophthalmol. *226*, 89–100. https://doi.org/10.1007/bf02172725.
35. Watson, P.G., and Young, R.D. (2004). Scleral structure, organisation and disease. A review. Exp. Eye Res. *78*, 609–623. https://doi.org/10.1016/s0014-4835(03)00212-4.
36. Summers, J.A. (2013). The choroid as a sclera growth regulator. Exp. Eye Res. *114*, 120–127. https://doi.org/10.1016/j.exer.2013.03.008.
37. Seo, S., Chen, L., Liu, W., Zhao, D., Schultz, K.M., Sasman, A., Liu, T., Zhang, H.F., Gage, P.J., and Kume, T. (2017). Foxc1 and Foxc2 in the Neural Crest Are Required for Ocular Anterior Segment Development. Invest. Ophthalmol. Vis. Sci. *58*, 1368–1377. https://doi.org/10.1167/iovs.16-21217.
38. Hay, E.D., and Zuk, A. (1995). Transformations between epithelium and mesenchyme: normal, pathological, and experimentally induced. Am. J. Kidney Dis. *26*, 678–690. https://doi.org/10.1016/0272-6386(95)90610-x.
39. Walker, H., Akula, M., and West-Mays, J.A. (2020). Corneal development: Role of the periocular mesenchyme and bi-directional signaling. Exp. Eye Res. *201*, 108231. https://doi.org/10.1016/j.exer.2020.108231.
40. Saika, S., Saika, S., Liu, C.Y., Azhar, M., Sanford, L.P., Doetschman, T., Gendron, R.L., Kao, C.W., and Kao, W.W. (2001). TGFbeta2 in corneal morphogenesis during mouse embryonic development. Dev. Biol. *240*, 419–432. https://doi.org/10.1006/dbio.2001.0480.
41. Fokina, V.M., and Frolova, E.I. (2006). Expression patterns of Wnt genes during development of an anterior part of the chicken eye. Dev. Dyn. *235*, 496–505. https://doi.org/10.1002/dvdy.20621.
42. Lan, Y., Ryan, R.C., Zhang, Z., Bullard, S.A., Bush, J.O., Maltby, K.M., Lidral, A.C., and Jiang, R. (2006). Expression of Wnt9b and activation of canonical Wnt signaling during midfacial morphogenesis in mice. Dev. Dyn. *235*, 1448–1454. https://doi.org/10.1002/dvdy.20723.
43. Shi, Z., Xu, J., Niu, L., Shen, W., Yan, S., Tan, Y., Quan, X., Cheung, E., Huang, K., Chen, Y., et al. (2023). Evolutionarily distinct and sperm-specific supersized chromatin loops are marked by Helitron transposons in Xenopus tropicalis. Cell Rep. *42*, 112151. https://doi.org/10.1016/j.celrep.2023.112151.
44. Schneider, C.A., Rasband, W.S., and Eliceiri, K.W. (2012). NIH Image to ImageJ: 25 years of image analysis. Nat. Methods *9*, 671–675. https://doi.org/10.1038/nmeth.2089.
45. Love, M.I., Huber, W., and Anders, S. (2014). Moderated estimation of fold change and dispersion for RNA-seq data with DESeq2. Genome Biol. *15*, 550. https://doi.org/10.1186/s13059-014-0550-8.
46. Chen, H., and Boutros, P.C. (2011). VennDiagram: a package for the generation of highly-customizable Venn and Euler diagrams in R. BMC Bioinf. *12*, 35. https://doi.org/10.1186/1471-2105-12-35.
47. Yu, G., Wang, L.G., Han, Y., and He, Q.Y. (2012). clusterProfiler: an R package for comparing biological themes among gene clusters. OMICS *16*, 284–287. https://doi.org/10.1089/omi.2011.0118.
48. Wickham, H. (2016). ggplot2: Elegant Graphics for Data Analysis (Springer International Publishing).

49. Kolde, R. (2012). Pheatmap: pretty heatmaps. R package version 1, 726.
50. Robinson, J.T., Thorvaldsdóttir, H., Winckler, W., Guttman, M., Lander, E.S., Getz, G., and Mesirov, J.P. (2011). Integrative genomics viewer. Nat. Biotechnol. *29*, 24–26. https://doi.org/10.1038/nbt.1754.
51. Zheng, R., Wan, C., Mei, S., Qin, Q., Wu, Q., Sun, H., Chen, C.H., Brown, M., Zhang, X., Meyer, C.A., and Liu, X.S. (2019). Cistrome Data Browser: expanded datasets and new tools for gene regulatory analysis. Nucleic Acids Res. *47*, D729–D735. https://doi.org/10.1093/nar/gky1094.
52. Shi, Z., Liu, G., Jiang, H., Shi, S., Zhang, X., Deng, Y., and Chen, Y. (2023). Activation of P53 pathway contributes to Xenopus hybrid inviability. Proc. Natl. Acad. Sci. USA *120*, e2303698120. https://doi.org/10.1073/pnas.2303698120.
53. Kim, D., Langmead, B., and Salzberg, S.L. (2015). HISAT: a fast spliced aligner with low memory requirements. Nat. Methods *12*, 357–360. https://doi.org/10.1038/nmeth.3317.
54. Anders, S., Pyl, P.T., and Huber, W. (2015). HTSeq–a Python framework to work with high-throughput sequencing data. Bioinformatics *31*, 166–169. https://doi.org/10.1093/bioinformatics/btu638.

STAR★METHODS

KEY RESOURCES TABLE

REAGENT or RESOURCE	SOURCE	IDENTIFIER
Antibodies		
RAD21	Abcam	Cat# ab217678;RRID: AB_2920658
AP2α	Abcam	Cat# Ab52222; RRID: AB_867683
AP2β	Immunoway	Cat# YN3852221094
AP2β	Abcam	Cat# Ab221094
PITX2	Abcam	Cat# Ab98297; RRID: AB_10887751
SOX10	Abcam	Cat# Ab155279; RRID: AB_2650603
P75	Proteintech	Cat# 55014-1-AP; RRID: AB_10858484
KERA	Bioss	Cat# bs-11054R
LUM	Abcam	Cat# Ab168348; RRID: AB_2920864
DCN	Abcam	Cat# Ab175404; RRID: AB_2890261
OCT4	Abcam	Cat# Ab18976; RRID: AB_444714
NANOG	Abcam	Cat# Ab80892; RRID: AB_2150114
PITX2	Abcam	Cat# Ab98297; RRID: AB_10887751
SOX10	Abcam	Cat# Ab155279; RRID: AB_2650603
VIM	Abcam	Cat# Ab8978; RRID: AB_306907
GAPDH	Sungene Biotech	Cat# LK9002
Bacterial and virus strains		
relief® 5α Chemically Competent Cell	tsingke	Cat# TSC-C01
Biological samples		
corneal ring	This paper	N/A
Chemicals, peptides, and recombinant proteins		
mTeSR1	STEMCELL	Cat# 85850
matrigel	Corning	Cat# BD354277
ReLeSR	STEMCELL	Cat# 100-0483
Y-27632	STEMCELL	Cat# 72302
DMEM/F12	Gibco	Cat# 11330032
KSR	Gibco	Cat# 10828028
MEM nonessential amino acids	Gibco	Cat# 11140050
retinoic acid	Sigma	Cat# 223018
bFGF	Proteintech	Cat# 78003.1
β-mercaptoethanol	Gibco	Cat# 21985023
ascorbic acid-2-phosphate	Sigma	Cat# 49752
Accutase	STEMCELL	Cat# 07920
Insulin-Transferrin-Selenium	Gibco	Cat# 41400045
Lipofectamine RNAiMAX	Invitrogen	Cat# 13778150
Opti-MEM	Gibco	Cat# 31985062
L-GlutaMAX	Gibco	Cat# 35050061
DAPI	Solarbio	Cat# C0065
RIPA buffer	Solarbio	Cat# R0010
phenylmethylsulfonyl fluoride	solarbio	Cat# P0100

(*Continued on next page*)

Continued

REAGENT or RESOURCE	SOURCE	IDENTIFIER
FuGENE	Promega	Cat# E2311
Dispase II	Roche	Cat# 04942078001
TRIzol	Invitrogen	Cat# 15596018CN
TritonX-100	Solarbio	Cat# 9002-93-1
Critical commercial assays		
Senescence-associated β-galactosidase staining	Cell Signaling	Cat# 9860
MiniBEST Universal RNA Extraction Kit	TaKaRa	Cat# 9767
PrimeScript RT reagent Kit	TaKaRa	Cat# RR037A
FastStart Universal SYBR Green Master	Roche	Cat# 4913714001
QIAquick PCR Purification Kit	Qiagen	Cat# 28104
Tanscript Aid T7 High Yield Transcription Kit	ThermoFisher Scientific	Cat# K0441
QIAquick Gel Extraction Kit	Qiagen	Cat# 28704
pEASY-Blunt zero Cloning Kit	TransGen Biotec	Cat# CB501-01
mMESSAGE mMACHINE SP6 Kit	ThermoFisher Scientific	Cat# AM1340
Deposited data		
Human corneal and scleral tissue transcriptome data	This paper	Database: https://ngdc.cncb.ac.cn/gsa-human/browse/HRA005702
hESC-derived differentiated cell transcriptome data	This paper	Database: https://ngdc.cncb.ac.cn/gsa-human/browse/HRA005733
Experimental models: Cell lines		
Human: Passage 48-52 H1 ES cells	Li et al.[22]	N/A
Experimental models: Organisms/strains		
Xenopus tropicalis: WT	Shi et al.[43]	N/A
Oligonucleotides		
Primers for Human sequences for qPCR, see Table S1	This paper	N/A
Probe for WISH, see Table S4	This paper	N/A
Recombinant DNA		
Plasmid: The human PCDHGC3 gene (NM_002588) was cloned into a GV230 vector between the *XhoI* and *KpnI* restriction sites.	This paper	N/A
Plasmid: The human WNT9B gene (NM_003396.3) was cloned into a H2317 vector between the *Eco RI and Eco RI* restriction sites.	This paper	N/A
Software and algorithms		
ImageJ	Schneider et al.[44]	https://imagej.nih.gov/ij/; RRID:SCR_003070
GraphPad Prism	GraphPad	https://graphpad-prism.cn; RRID:SCR_002798
HISAT2	Johns Hopkins University	http://daehwankimlab.github.io/hisat2/; RRID:SCR_015530
DESeq2	Love et al.[45]	RRID: SCR_015687
VennDiagram	Chen et al.[46]	VennDiagram (RRID:SCR_002414)
clusterprofiler	Yu et al.[47]	clusterProfiler (RRID:SCR_016884)
ggplot2	Wickham et al.[48]	ggplot2 (RRID:SCR_014601)
pheatmap	Kolde et al.[49]	pheatmap (RRID:SCR_016418)
IGV	Robinson et al.[50]	https://igv.org
Cistrome Data Browser database	Zheng et al.[51]	http://cistrome.org/db/

RESOURCE AVAILABILITY

Lead contact

Further information and requests for resources should be directed to and will be fulfilled by the lead contact, Bi Ning Zhang (zbnxtt@gmail.com).

Materials availability

This study did not generate new unique reagents.

Data and code availability

- Transcriptome data have been deposited at the Genome Sequence Archive (GSA for human, https://ngdc.cncb.ac.cn/gsa-human/) and are publicly available as of the date of publication. The accession number for the raw data files are HRA005702 and HRA005733.
- This paper does not report original code.
- Any additional information required to reanalyze the data reported in this paper is available from the lead contact upon request.

EXPERIMENTAL MODEL AND STUDY PARTICIPANT DETAILS

The wild-type males and females used for breeding are all adult *X. tropicalis* that have been reared for over a year. *X. tropicalis* must be maintained on a regular light/dark cycle. The light and dark periods in the laboratory Xenopus room are each set to 12 hours. The temperature for the growth and reproduction of Xenopus is controlled between 22°C-28°C. Animal ethics approval for this study was obtained from the Animal Ethics Committee of the Eye Institute of Shandong First Medical University (SDSYKYJS No.20220416).

The human embryonic stem cell line H1 (hESC) was cultured in serum-free medium mTeSR1 on plates coated with Matrigel. The cells were incubated at 37°C in a humidified atmosphere containing 5% CO_2. The medium was changed daily.

Four human corneal rings were obtained from the Eye Bank of the Eye Hospital of Shandong First Medical University within 7 days of the corneal donation. The study was approved by the Ethics Committee of Eye Hospital of Shandong First Medical University (R202103030107). Consents were obtained for research purposes prior of the study. This study was conducted in compliance with the tenets of the Declaration of Helsinki.

METHOD DETAILS

Neural crest cells and corneal keratocyte differentiation

The NCC differentiation was conducted as previously described.[22] hESC were plated on 1% matrigel-coated dishes and allowed to reach 30% confluent after 3 days, with each clone consisting of approximately 80-100 cells. Subsequently, the cells were cultured in neural crest differentiation medium (NDM) for 5 days. NDM comprises DMEM/F12 (Gibco, USA), 20% knockout serum replacement (KSR, Gibco, UAS), L-GlutaMAX (2 mM, Gibco, USA), MEM nonessential amino acids (0.1 mM, Gibco, USA), β-mercaptoethanol (0.1 mM, Gibco, USA), basic fibroblast growth factor (4 ng/mL, bFGF, proteintech, Wuhan, China), and 1 μM retinoic acid (RA, Sigma, Missouri, USA). The medium was changed daily.

For corneal keratocyte differentiation, hESC-derived NCCs were treated with Accutase (STEMCELL Technology, Canada) and then plated on 1% matrigel-coated plates. They were subsequently exposed to keratocyte differentiation medium for 21 days. This medium consists of DMEM/F12, 10 ng/mL bFGF, 1 mM ascorbic acid-2-phosphate (Sigma, Missouri, USA), 1% Insulin-Transferrin-Selenium (ITS, Gibco, USA), and 1% MEM nonessential amino acids. The medium was changed every two days.

siRNA knockdown

RAD21 mRNA, *PCDHGC3* mRNA and *WNT9B* mRNA were knocked down using siRNA obtained from Guangzhou RiboBio Co., Ltd. (Guangzhou, China). For each well of a six well plate, 9 μL Lipofectamine RNAiMAX (Invitrogen, USA) and siRNA (90 nM) were dissolved in 250 μL Opti-MEM (Gibco, USA), incubated for 5-10 minutes, and added to the wells. The medium was changed 24 hrs after transfection.

SA-β-gal staining

Senescence-associated β-galactosidase staining (SA-β-gal) was performed according to the manufacturer's protocol (Cell Signaling Technology, USA) with NCCs differentiated into keratocytes for two weeks. The cells were fixed for 15 minutes in the culture dish, washed twice with phosphate-buffered saline (PBS), and incubated with the β-gal staining solution overnight at 37°C.

Quantitative real-time PCR (qPCR)

Total RNA was extracted from differentiated cells at different time points after differentiation using the MiniBEST Universal RNA Extraction Kit (TaKaRa, Tokyo, Japan). The concentration and purity of the RNA were measured using a NanoDrop One spectrophotometer (Thermo Fisher Scientific, USA). Complementary DNA (cDNA) was synthesized with the PrimeScript RT reagent Kit (Perfect Real Time) (RR037A, Takara Bio

Inc., Japan). qPCR was performed using FastStart Universal SYBR Green Master (4913714001, Roche, Switzerland). The primers used are listed in Table S1. Gene expression levels were normalized to GAPDH.

Immunocytochemistry

Cells were fixed with 4% paraformaldehyde for 15-20 minutes and washed three times with PBS. Depending on the predicted expression location of the target protein, cells were permeabilized using different concentrations of Triton (Solarbio, Beijing, China) and then washed three times with PBS. After blocking with 5% goat serum (AR0009, Wuhan, China) for 30 minutes, cells were incubated overnight with primary antibody (listed in Table S2) at 4°C. Second antibodies used were Alexa Fluor 488 or Alexa Fluor 594 (1:500, Abcam, UK). Finally, DAPI (Solarbio, Beijing, China) staining was performed for observation. Images were captured using a fluorescence microscope (Echo Laboratories, USA and Keyence, China).

Western blot

NCC and keratocytes lysates were prepared using RIPA buffer (Solarbio, Beijing, China) supplemented with 1% phenylmethylsulfonyl fluoride (PMSF, solarbio, Bijing, China). 100 μL lysate was added to each well of a 6-well plate and incubated for 15 minutes on ice. The lysate was collected by scraping the cells with a 1 mL pipette tip and transferred to a 1.5 mL centrifuge tube. After centrifugation at 13,523 g for 20 minutes at 4°C, the supernatant was collected and mixed with 5 × loading buffer. The mixture was heated at 95°C for 10 minutes. The samples could be directly used for Western blot or stored at -80°C for later use.

For Western blot analysis, protein samples were subjected to 10% acrylamide gel electrophoresis and transferred to polyvinylidene difluoride membranes for antibody incubation. Primary antibody incubated at 4°C overnight (listed in Table S3) and GAPDH antibody (1:1000, LK9002, Tianjin Sungene Biotech Co., Ltd, China) was used as a loading control. The protein bands were quantified using ImageJ 6.1.0 software (USA) by analyzing the grayscale image peaks, involving the selection of bands with the rectangle tool after inverting the images to the 8-bit format.

Transwell assay

Cells were transfected with siRNA for 3 days, then digested using accutase. Cells were subsequently resuspended at a concentration of 2×10^5 cells in 100 μL of NDM containing 2% KSR, and gently added to the upper chamber. The lower chamber was filled with 600 μL of NDM containing 20% KSR. After 24 hrs, the upper chamber was removed, and cells were fixed with 4% paraformaldehyde for 20 mins, followed by washing with PBS. The cells were then stained with crystal violet for 20 mins. After PBS rinsing, images were captured using a microscope (Echo Laboratories, USA), and the number of migrated cells was counted using ImageJ.

Scratch assay

The scratch wound healing assay was used to access cell migration capacity. In each well of a 6-well plate coated with Matrigel, 4×10^5 NCCs were seeded, with the culture medium supplemented with 10 μM Y-27632. Transfection with siRNA occurred once cells reached 80% confluence. Three days post-transfection, when cell proliferation reached 90%-100%, a scratch assay was performed using a 10 μL pipette tip. Images were captured at 0 hr, 12 hrs, and 24 hrs at the same location. The scratched areas were measured using ImageJ.

Overexpressing plasmid construction and transfection

The human PCDHGC3 gene (NM_002588) was cloned into a GV230 vector between the *XhoI* and *KpnI* restriction sites (GENE, China). The human WNT9B gene (NM_003396.3) was cloned into a H2317 vector between the *Eco RI and Eco RI* restriction sites (OBIO, China). A vector with a nonsense sequence inserted served as the negative control. Plasmids of 1 mg were transfected into 1×10^5 NCCs using 2.5 μL FuGENE (Promega, USA).

Isolation of corneal stroma and scleral stroma

Human cornea and sclera are separated from the corneal ring using corneal scissors (MR-S221A, Suzhou, China). The scleral stroma was further separated from the epithelium and the attached iris using suture ligature forceps (MR-F101A-3, Suzhou, China). The corneal stroma was separated from the endothelium using suture ligature forceps, and the epithelium was removed by digestion of the sample with 2.4 U/mL of Dispase II (Roche, Switzerland) at 37°C for 1 hr.

RNA sequencing

RNA sequencing of human corneal stromal tissue, human scleral stromal tissue, NCC-induced keratocytes knocked down for RAD21, NCC-induced keratocytes overexpressing PCDHGC3, untreated NCC-induced keratocytes. Total RNA was extracted using the TRIzol reagent (Invitrogen, CA, USA) according to the manufacturer's protocol. RNA purity and quantification were evaluated using the NanoDrop 2000 spectrophotometer (Thermo Scientific, USA). RNA integrity was assessed using the Agilent 2100 Bioanalyzer (Agilent Technologies, Santa Clara, CA, USA). The libraries were constructed using VAHTS Universal V6 RNA-seq Library Prep Kit according to the manufacturer's instructions. The transcriptome sequencing and analysis were conducted by OE Biotech Co., Ltd. (Shanghai, China).

In vitro transcription and microinjection with *X. tropicalis* embryos

The pCS2-*wnt9b* plasmid was linearized by *NotI* digestion. *In vitro* transcription of the plasmids was conducted with mMESSAGE mMACHINE SP6 Kit (ThermoFisher Scientific, USA). The resulting mRNAs were purified with RNeasy Mini Kit (Qiagen, Germany). For microinjection, 200 pg of *wnt9b* mRNA and 100 pg of GFP mRNA were injected into a single *X. tropicalis* cell on the dorsal side of blastomere at the 2-cell stage.

Whole-mount *in situ* hybridization (WISH)

Digoxigenin-labeled RNA probes for *in situ* hybridization were generated using PCR primers listed in Table S4. The primers were designed to amplify specific regions of the target genes, with the reverse primer modified to include the T7 promoter sequence (5'-TAATACGACTCAC-TATAGGG-3'). After purification, *in vitro* transcription was performed. The staining protocol for WISH followed the established protocol.[52]

Vibratome section

Following WISH, stained embryos were subjected to vibratome sectioning for signal detection. A 1:9 mixture of 25% glutaraldehyde was added to a gelatin/albumin embedding medium (22.5 mL 10 × PBS, 1.1 g gelatin, 67.5 g albumin, 225 mL water) and thoroughly mixed. The mixture was poured into embedding molds. Each embryo was transferred to a mold with the head facing upward and both eyes kept in the same plane. After solidification at room temperature, the sample-containing gel blocks were attached to the metal blocks of a vibratome (Leica, Wetzlar, Germany). Sections of 30 μm thickness were obtained. ImageJ software was used to measure the positive *pitx2* staining area in the periorbital region. A paired t-test was used to compare the *pitx2* staining areas between control eyes and eyes with target gene overexpression.

QUANTIFICATION AND STATISTICAL ANALYSIS

Bioinformatics analysis

The libraries were sequenced on an Illumina Novaseq 6000 platform and 150 bp paired-end reads were generated. Reads were aligned to the human reference genome (GRCh38.p13) using HISAT2,[53] and gene expression levels were quantified. HTSeq-count was employed to determine read counts for each gene.[54] DESeq2[45] software was employed for differential gene expression analysis, where genes with q-value < 0.05 and absolute log2 (foldchange) > 1 were defined as DEGs. The DEGs were subjected to hierarchical clustering analysis using pheatmap[49] to visualize their expression patterns under different conditions. Enrichment analysis of gene ontology (GO) and KEGG pathway terms for DEGs was carried out using the hypergeometric distribution algorithm. VennDiagram[46] was employed to illustrate the intersection of DEGs with the canonical WNT signaling pathway across various conditions. The intersection of different gene sets was visualized using ggplot2[48] R package. Additionally, gene set enrichment analysis was conducted using clusterprofiler package.[47]

Statistical analyses

All experiments were repeated for at least three times. Statistical analysis was performed using GraphPad Prism 9.5.0 software (USA). We employed the paired sample T-test for quantitative analysis to compare the *pitx2*-positive regions between the control eyes and the *wnt9b* overexpressing periorbital mesenchyme and conducted a Fisher's exact test to compare the number of embryos with abnormal migration of NCCs (*ap2a* and *twist1* staining) between the self-control group and the ovWNT9b group. Comparisons between the two groups in all the other experiments were assessed using the Student's T-test. Data are presented as mean ± standard deviation. $*P < 0.05$, $**P < 0.01$, $***P < 0.001$. ns, no significance.